Metals & corrosion

Microstructural evolution in Cu–Nb processed via friction consolidation

Mageshwari Komarasamy[1,*] ⓘ, Xiao Li[1], Scott A. Whalen[1], Xiaolong Ma[1], Nathan Canfield[1], Matthew J. Olszta[1], Tamas Varga[2], Alan L. Schemer-Kohrn[1], Anqi Yu[3], Nicole R. Overman[1], Suveen N. Mathaudhu[1,3,4], and Glenn J. Grant[1]

[1] Energy and Environment Directorate, Pacific Northwest National Laboratory, Richland, WA, USA

[2] Environmental Molecular Sciences Laboratory, Pacific Northwest National Laboratory, Richland, WA, USA

[3] Materials Science and Engineering Program, University of California, Riverside, CA, USA

[4] Mechanical Engineering Department, University of California, Riverside, CA, USA

ABSTRACT

Immiscible alloys, whether in well-mixed or layered forms, are of increasing interest based on their novel structural and functional properties, such as enhanced thermal stability against grain growth or radiation-induced defect trapping at the interfaces. To address the need for new approaches to tailor microstructures, the microstructural development of an immiscible Cu-4 wt.% Nb alloy processed via friction consolidation of elemental powders is investigated. Friction consolidation is a solid phase processing technique that imparts severe plastic strain into a deforming volume resulting in elevated temperatures below the melting temperature of the alloy. Two distinct processing pathways were chosen to understand the effect of thermomechanical conditions on the final microstructure. The microstructure was characterized using scanning electron microscopy, scanning transmission electron microscopy, and X-ray diffraction techniques. Path 1 exhibited larger strain, strain rate, and temperature as compared with path 2. In path 1, agglomerated Nb particles were present in the recrystallized ultrafine-grained Cu matrix, while in path 2 extremely fine and dispersed Nb particles were present in a highly deformed Cu matrix. In both pathways, supersaturation of Cu in Nb lattices was noted, but not vice versa. The asymmetry in mixing is explained based on deformation-based, thermodynamic and kinetic factors. These findings provide a pathway for creation of novel tailored microstructures and improved properties in any number of binary immiscible alloy systems.

Introduction

Growing interest towards Cu-based immiscible alloy systems is due mainly to the exceptional properties such as thermal stability [1], creep resistance [2], strength [3], irradiation resistance [4], and furthermore, these alloys can be used as an excellent model system to investigate the forced mixing and microstructural evolution under various severe plastic deformation conditions. To that end, elements such as Ag, Fe, Nb, Ta, Cr, W, and Mo that have limited solubility in copper are generally forcibly distributed in supersaturated solid solution via either severe plastic deformation techniques or rapid solidification methods. Forced mixing under extreme plastic deformation depends primarily on the co-deformation extent of the constituent elements, positive heat of mixing and crystal structure. Extensive experimental [5–14] and simulation [15–23] work has been conducted to understand the effect of these inherent factors on alloy formation in multiple immiscible alloys systems. For instance, Ashkenazy et al. [16] investigated the shear-induced chemical mixing in Cu–X (X = Cu, Ag, Fe, Nb, and V) systems using molecular dynamics (MD) simulations. In the case of Cu-FCC systems, the Ag and Ni particles were reported to dissolve via a superdiffusion mechanism, while Cu–Nb and Cu–V did not show considerable material movement across the Cu-BCC interface. Friction stir processing of Cu-based systems under comparable experimental conditions exhibited increased forced mixing compared in Cu-5 wt.%. Fe compared to Cu-5 wt.%. Cr [5]. Similar results were observed in high-pressure torsion (HPT) [7] and mechanical alloying [8] experiments involving Cu-based immiscible systems. Various mechanisms have been proposed to explain the formation of miscible alloys from immiscible systems under severe plastic deformation conditions [24, 25], including defect-assisted (vacancies, dislocations, and grain boundaries) diffusion [24–27] and ballistic superdiffusion [15–17, 28, 29]. However, as will be presented herein, multiple factors contribute collectively to achieving extended solubility in immiscible systems.

The microstructure of the severe plastically deformed Cu-based immiscible alloys generally consists of a nanocrystalline/ultrafine-grained copper matrix with the immiscible elements in the form of fine precipitates/particles and/or as supersaturated solid solution with copper. Extensive microstructural refinement is generally noted when Cu-based immiscible alloys are processed via friction stir processing [13, 30], wire drawing [10, 14], HPT [9, 11, 31], mechanical alloying [8], and accumulative roll bonding [32]. Furthermore, post-processing aging treatments typically result in the formation of nano-sized precipitates that provide grain boundary pinning (Zener pinning) and obstacles to the dislocation motion [13]. In addition to kinetic factors such as Zener pinning, thermodynamic effects such as grain boundary energy minimization via solute segregation and solute drag generally lead to extreme stability against grain growth [1]. Furthermore, the presence of metastable Ta precipitates in a nanocrystalline Cu–Ta alloy was shown to provide creep resistance up to $0.65 \, T_m$ via grain boundary pinning [2]. A review article by Ma [33] addresses alloy formation in various immiscible systems via several non-equilibrium processing methods, and a review article by Suryanarayana [34] mainly discusses the non-equilibrium alloy formation via mechanical alloying. Among various Cu-based immiscible alloy systems, Cu–Nb is among the most investigated and exhibits limited mutual solubility. For instance, at 973 K, the maximum solubility of Cu in Nb is about 0.15 at.%, while Nb solubility in Cu is less than 0.01 at.% [35]. Due to their limited solubility, conventional casting methods usually result in limited Nb in solid solution with Cu and Nb is generally present as coarse primary particles in the Cu [36].

Among many advanced manufacturing methods, solid phase processing (SPP) techniques, such as shear assisted processing and extrusion (ShAPE) [37–41], friction consolidation (FC) [42–44], friction extrusion (FE) [35, 45, 46], and friction stir processing (FSP) [47], are gaining momentum due to the extraordinary microstructures leading to exceptional properties in various alloy systems. Furthermore, FSP of Cu–Ag–Nb [13] and Cu–Al–Nb [30] immiscible systems have been carried out to introduce deformation-induced shear mixing. In both cases, forced mixing and the subsequent precipitation of second phases were noted. These results reveal that FSW/P could in fact be utilized to impart extreme deformation into the deforming material volume to ultimately force the mixing of the immiscible components. In addition to forced mixing, FSW/P and similar techniques could potentially be used to produce persistently metastable second phases.

Initial investigations have shown the potential of FC and FE methods to fabricate bulk structures with microstructure and properties not observed in conventional extrusion and consolidation methods. However, the understanding of the imposed deformation conditions and the corresponding microstructural evolution is lacking. The deformation conditions can be significantly varied via processing input variables such as tool rotational speed, die advance rate, axial load, and external cooling to introduce variability in the evolved microstructure. Table 1 shows an example of two distinct heuristic pathways with varying strain, strain rate, and the resultant temperature of the deformation volume for two processing paths presented in Table 2.

In this study, the microstructural evolution of Cu–Nb consolidated via two distinct pathways is investigated. To that end, microscopy techniques such as scanning electron microscopy (SEM) and scanning transmission electron microscopy (STEM) are utilized to probe the microstructural evolution as a function of processing pathway. Path 1 exhibits refined Nb particles and ultrafine-grained Cu grains, while path 2 results in severely deformed Cu and Nb phases. The presented findings provide an improved understanding of the microstructural evolution in Cu–Nb alloy under high temperature severe plastic deformation conditions.

Materials and methods

Elemental Cu (99.5%) and Nb (99.9% purity) powders were procured from Alfa Aesar (Massachusetts USA). The elemental powders in the nominal composition of Cu-4 wt.% Nb were weighed and mixed using a roller mixer. A ShAPE manufactured by BOND Technologies, Inc. was used to execute the friction consolidation of the powder mixture. The overall setup of the friction consolidation process is presented in Fig. 1. Figure 1a shows the consolidation die on the left and the water-cooled container

assembly on the right. The Cu–Nb powder mixture was cold pressed into a powder chamber at 176 MPa using a hydraulic press. The inner diameter of the H13 tool steel chamber was 26.0 mm. The powder compact was then fit onto the container assembly as shown in Fig. 1a. The inset in Fig. 1a shows the top view of the consolidation die. The consolidation die with an outer diameter of 25.4 mm was fabricated from MP159, a Co-based superalloy. The die face consisted of two spiral grooves that converged towards the center. Temperature was measured using a K-type thermocouple located at 4.2 mm radially from the center of the die and 1 mm beneath the root of the scroll groove. The details on the two distinct processing conditions are presented in Table 2 in order to impose the qualitative conditions described in Table 1. The schematic in Fig. 1b captures the friction consolidation process and various process variables. The tool rotated at certain rpm while the container assembly advanced pushing the material against the die. As noted in Table 2, the forge force in path 2 was initially increased to 75 kN and then the rotation of the die was initiated, while on other hand in path 1, the die was rotated at 200 rpm and then moved in contact with the cold compacted powder. The abort temperature in the last column denotes the temperature at which the consolidation processes were stopped. In both paths, argon gas cover was utilized to avoid oxidation. Further details on the friction consolidation processes can be found in Refs. [42, 43].
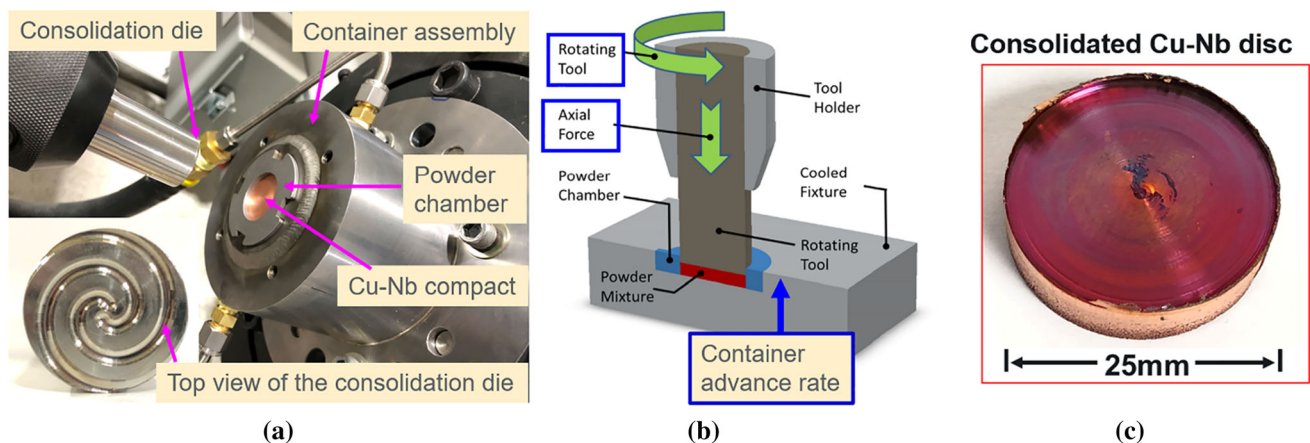
The outcome of the friction consolidation process was a cylindrical disk (Fig. 1c). For the various microstructural analyses, the disk was cross-sectioned along the length, mounted in epoxy and polished to a surface finish of ∼ 0.05 μm using colloidal silica suspension. Light microscopy analysis (in bright field mode) of the cross-section was conducted using an Olympus BX51M metallurgical microscope. SEM and energy-dispersive X-ray spectroscopy (EDS) analyses, in addition to specimen preparation for transmission electron microscopy (TEM) analysis, were conducted using focused ion beam (FIB) milling on a FEI Quanta 3D field emission gun dual beam FIB/SEM. Electron backscatter diffraction (EBSD) analyses were completed using a JEOL JSM-7001F field emission SEM equipped with a Bruker x-flash|60 EDS detector and a Bruker e-flash HD EBSD detector. Analysis of EBSD was completed with the Bruker Esprit 2.1 software package. STEM

Table 1 Key difference in deformation conditions between paths 1 and 2

	Strain	Strain rate	Temperature
Path 1	High	High	High
Path 2	Low	Low	Low

Table 2 Summary of the friction consolidation processing parameters

Processing conditions	Die rotational speed (RPM)	Container advance rate (mm/min)	Starting forge force (kN)	Abort temperature (K)
Path 1	200	2	0	883
Path 2	25	1	75	523

Figure 1 **a** Setup of the friction consolidation process, **b** schematic of the consolidation process with selected process variables, and **c** an image of the processed Cu–Nb consolidate. (For color coding please refer to the online version).

analysis was performed at 200 keV using an aberration, probe-corrected JEOL ARM 200CF microscope equipped with a JEOL Centurio silicon drift detector (SDD) for EDS analysis, and high-angle annular dark field (HAADF) and STEM bright field (BF) detectors. STEM-HAADF images were collected using a convergence angle ranging from 27 mrad (1.55°) and a collection angle between 68–230 mrad (3.90–13.18°), and STEM-BF images were collected using a convergence angle of 6.9 mrad (0.40°) and a collection angle of 14 mrad (0.80°). STEM-EDS data acquisition and analysis was performed with a convergence angle of 34.4 mrad (1.97°) and a collection angle between 110–440 mrad (6.3–25.2°) and Pathfinder^{TM} X-ray Microanalysis Software. Microbeam X-ray diffraction (μXRD) analysis was carried out using a Rigaku D/Max Rapid II micro-diffraction system equipped with a 2D image plate detector. X-rays were generated with a MicroMax 007HF generator fitted with a rotating Cr anode (λ = 2.2897 Å) and focused on the specimen through a 300-μm-diameter collimator. The incident angle was oscillated between 15 and 25° ω, and the sample was oscillated in its horizontal plane between − 10 and 10° φ. 2DP, Rigaku 2D Data Processing Software (Ver. 1.0,

Rigaku, 2007), was used to integrate the diffraction rings captured by the detector. Analysis of the diffraction data was carried out using JADE 9.5.1 (Materials Data, Inc.). TOPAS software (v5, Bruker AXS, Germany) was used for lattice parameter analysis with crystal structures obtained from the Inorganic Crystal Structure Database (Fachinformationszentrum Karlsruhe, Germany).

Results

Starting powder analysis

Morphological analyses of the Cu and Nb elemental powders in the as-received condition are presented in Fig. 2. Figure 2a$_1$, b$_1$ shows the powder morphology, while Fig. 2a$_2$, b$_2$ shows the backscattered electron (BSE)-SEM images of the cross-section of the polished powders. The Cu powder consists of both porous and solid particles as marked by the solid and dotted arrows. The particle sizes of the Cu and Nb powders are 240 ± 92 and 120 ± 47 μm, respectively. Inverse pole figure (IPFx) orientation mapping of the Cu and Nb particles is presented as an inset in Fig. 2a$_2$, b$_2$, respectively. Based on the EBSD analysis, the grain
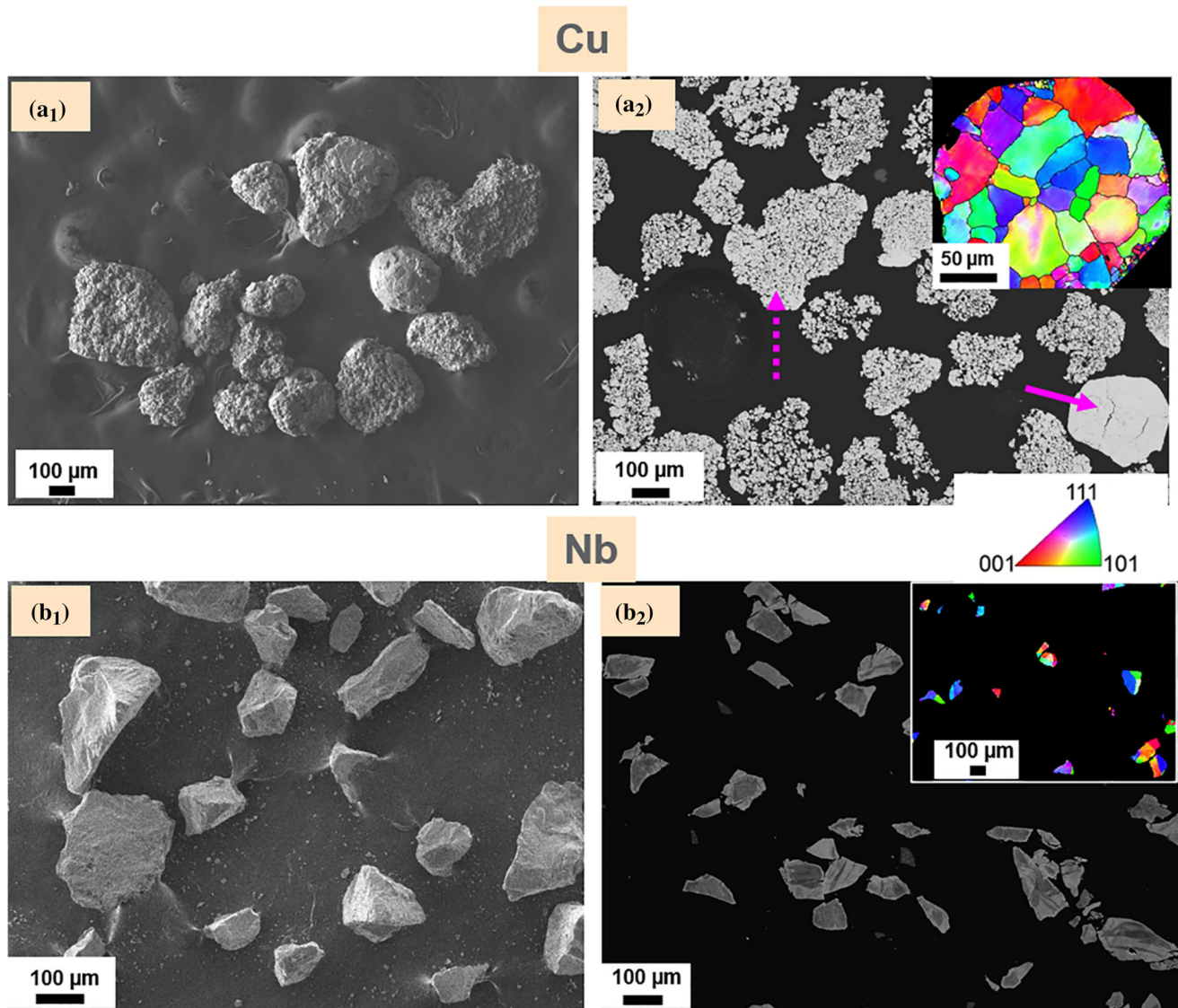
Figure 2 Microstructural analysis of the as-received Cu powder (**a₁**, **a₂**) and Nb powder (**b₁**, **b₂**). **a₂, b₂** show the cross-sectional microstructure of the polished powders. Inset in (**a₂**) and (**b₂**) shows IPF-Z grain orientation map of Cu and Nb particles. (For color coding, please refer to the online version).

size of the Cu and Nb particles is 1–100 μm and 1–120 μm, respectively.

Deformation output

The measured approximate tool temperature as a function of the processing time for the two paths is presented in Fig. 3a. Path 1 exhibits a high temperature compared with path 2 due mainly to the higher die rotational speed and faster container advance rate that introduced large strain and strain rate into the deforming volume. The measured tool temperature is the net effect of heat generation due primarily to: (1) frictional and adiabatic heating due to the interaction between the tool and deformation volume, (2) the interaction between the die and the container wall, and the heat loss (3) through the die to the spindle assembly and (4) to the container assembly which has water cooling. While the contribution from all four factors will be different for paths 1 and 2, it is certain that the higher rotational speed and advance rate dominate and will result in faster temperature rise.
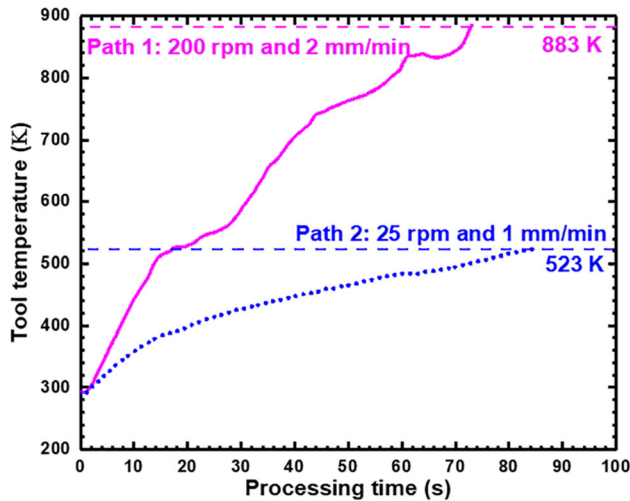
Figure 3 Measured tool temperature with increasing processing time for the two deformation pathways.

Path 1 microstructural characterization

Figures 4 and 5 show the microstructural evolution in path 1 analyzed via SEM and STEM techniques, respectively. Figure 4a shows the light micrograph of the vertical cross-section of the consolidate, indicating that the processing depth is nominally 3.90 mm. Analysis locations for the processed and unprocessed regions, the boundary separating the two regions, and SEM and EDS analyses are all marked on the image (Fig. 4a). Furthermore, the inset in Fig. 4a shows coarse Nb particles in the unprocessed region. In the SEM-BSE micrograph, Nb particles appear brighter than Cu particles due to the higher atomic number of the former. Figure $4b_1$, b_2 and c_1, c_2 shows the microstructural evolution inside the processed region, while Fig. $4d_1$–d_3 shows the microstructural
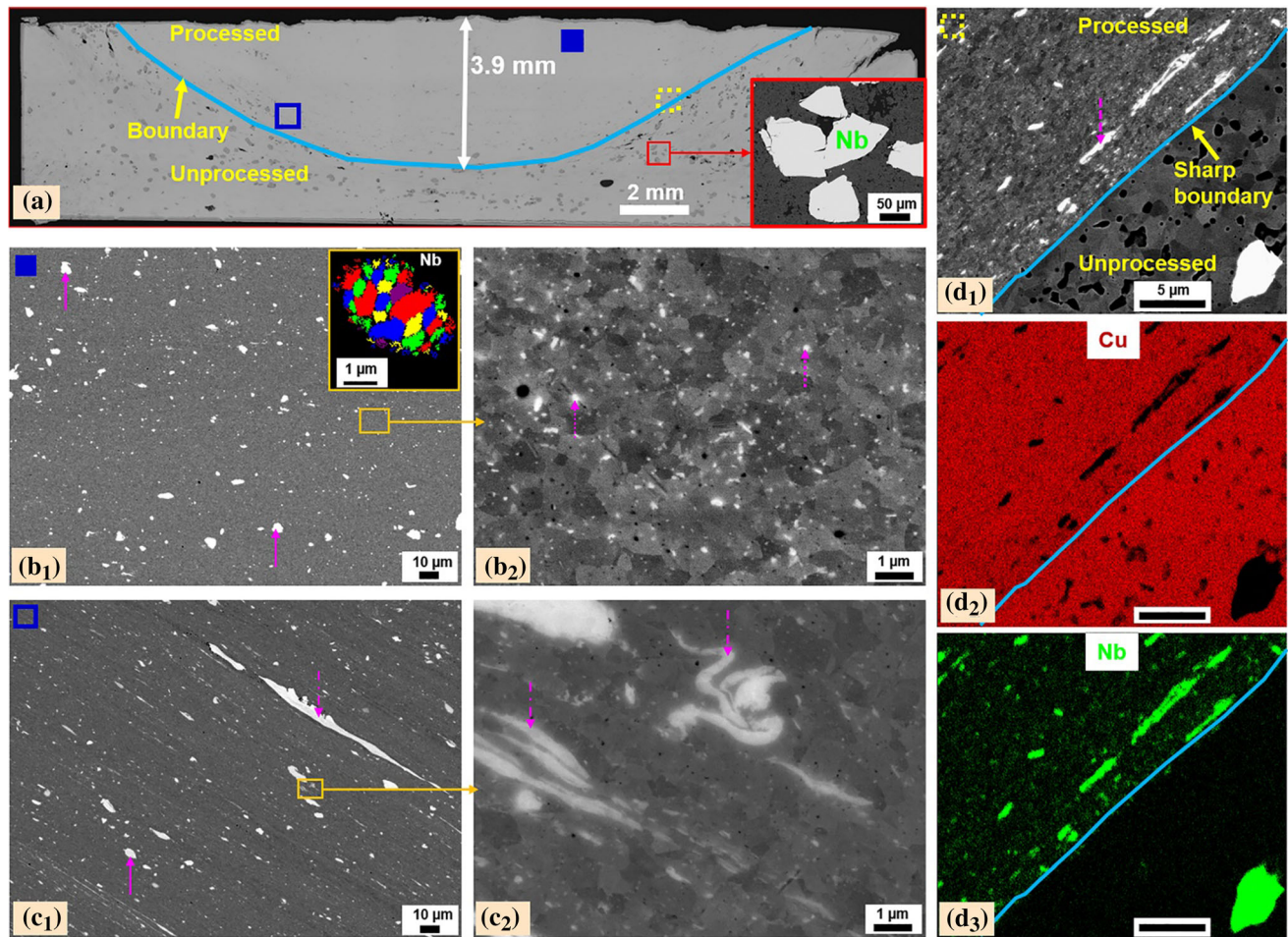

Figure 4 Microstructural analysis of friction consolidated sample processed via path 1. **a** Optical microscopy image showing the cross-section, BSE-SEM images b_1, b_2 from interior of the processing region, c_1, c_2 adjacent to the boundary, and d_1 across the boundary. SEM–EDS maps of d_2 Cu and d_3 Nb elements across the boundary. (For color coding please refer to the online version).
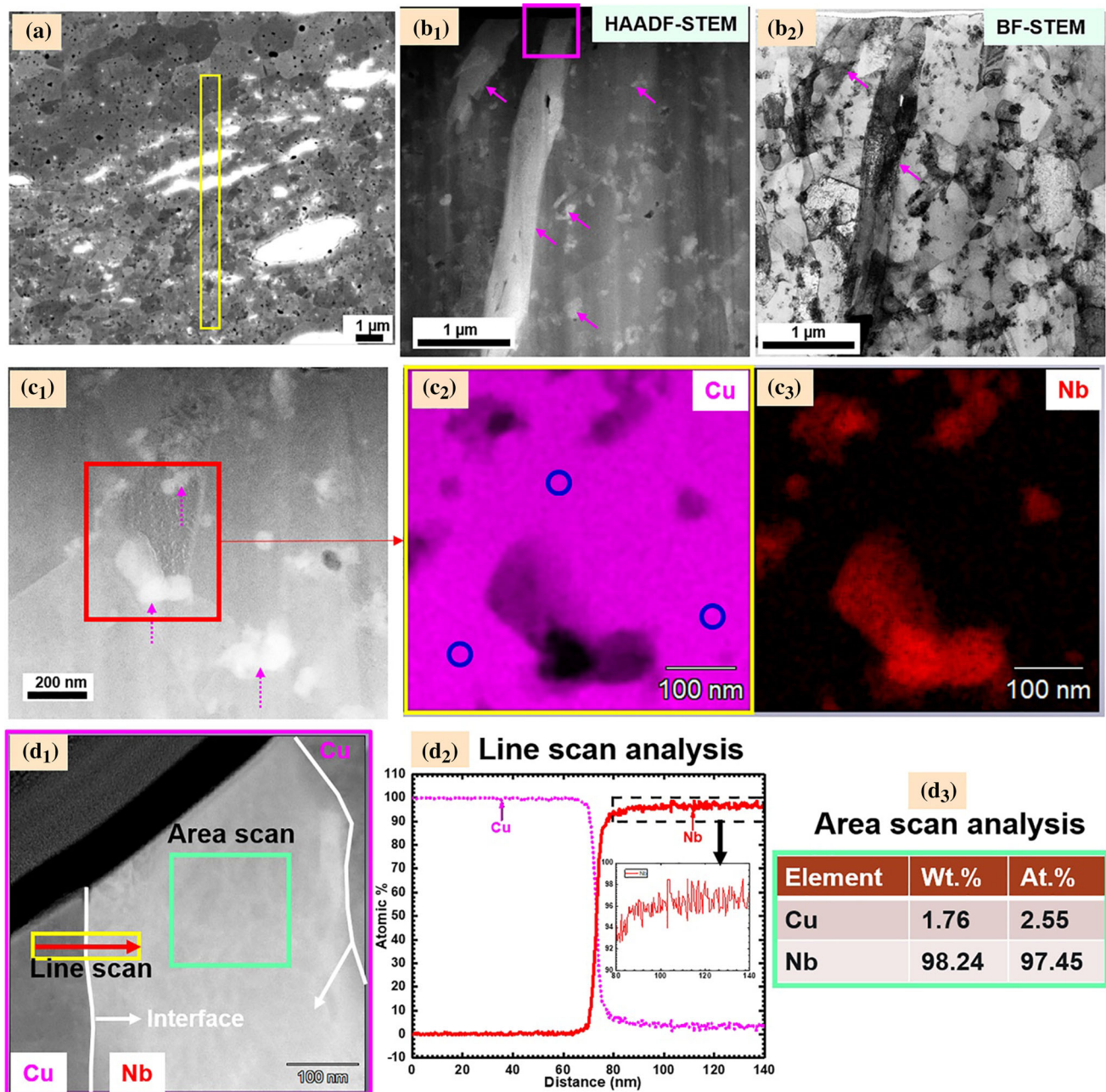
Figure 5 **a** Location of the FIB sample presented on a SEM-BSE image; overview images of the STEM foil in **b₁** HAADF and **b₂** BF conditions showing various length scales of Nb particle. **c₁** High-magnification STEM-HAADF image with the corresponding EDS map of **c₂** Cu and **c₃** Nb revealing the nature of the sub-micron scale Nb particles. **d₁** STEM-EDS line and area scan features across the boundary. Both micrometer and sub-micrometer dimension Nb particles are observed in the processed region as denoted by the solid and dotted arrows, respectively. There is a significant reduction in the Nb particle size in the processed details are presented on a HAADF image consisting of Cu and Nb phases, and the corresponding results **d₂** EDS line scan results across the Cu/Nb phase boundary and **d₃** area scan on the Nb particle are also shown. (For color coding, please refer to the online version).

region (sizes less than 100 nm, Fig. 5c₁) compared with the unprocessed region (sizes of 1–200 μm). A EBSD-based grain map of a micrometer-sized Nb particle is presented as an inset in Fig. 4b₁. The grain size of the Nb particle is nominally 0.4–0.6 μm, and

most of the micrometer-sized Nb particles exhibit equiaxed fine/ultrafine (< 1 μm) grains. Additionally, elongated Nb particles of varying thickness are observed adjacent to the boundary between the processed and unprocessed region, as shown by dash-dotted arrows in Fig. 4c$_1$, c$_2$, and d$_{1-3}$. These elongated Nb particles are observed only near the boundary, while the remainder of the processing volume consists predominantly of micrometer- and sub-micrometer-sized Nb particles. As noted from Fig. 4d$_1$–d$_3$, the boundary between processed and unprocessed regions is sharp, and the nature of the Nb particles approaching the interface changes with distance. For instance, a Nb particle that is 10 μm from the boundary is intact, while Nb particles neighboring the boundary have sustained significant deformation and elongation. This can be clearly noted from the Nb EDS map presented in Fig. 4d$_3$. Furthermore, regions with sub-micrometer Nb particles exhibit ultrafine Cu grains due to effective grain boundary pinning. For instance, the average Cu grain size near the boundary is ∼ 2.3 μm, while sub-micrometer (∼ 0.7 μm) grains are observed in the interior of the processing region. Overall, significant plastic deformation, fracture, further plastic deformation, and continuation of this cycle have led to the appreciable refinement in both the Cu grains and Nb particles.

STEM analysis of the evolved microstructure is presented in Fig. 5 with the location of the FIB sample on a SEM-BSE image displayed in Fig. 5a. The STEM sample was taken close to the boundary so that the analysis of both fine-scale and elongated Nb particles could be made. The overview STEM-HAADF and STEM-BF images presented in Fig. 5b$_1$, b$_2$, respectively, show the presence of coarse elongated and sub-micrometer Nb particles (marked by solid arrows), and ultrafine Cu grains. The size, location, and distribution of the sub-micrometer-sized Nb particles can be seen in the high-magnification STEM-HAADF image shown in Fig. 5c$_1$ and in the STEM-EDS area map of Cu and Nb presented in Fig. 5c$_2$, c$_3$. Fine-scale, intergranular and transgranular Nb particles are observed in these images. The majority of sub-micrometer Nb particles appear to be clustered and are denoted by dotted arrows. Nb is not observed to be present as solid solution in the Cu matrix; the STEM-EDS spot analysis denoted by open circles in Fig. 5c$_2$ indicates 100% Cu. Furthermore, line scan analysis across the Cu/Nb phase boundary

and an area scan inside the Nb particle (the location is marked by open rectangle in Fig. 5b$_1$) are presented in Fig. 5d$_1$–d$_3$. The phase boundary was oriented edge on to the electron beam to avoid projection issues. The line scan result across the Cu/Nb interface in Fig. 5d$_2$ reveals the presence of Cu in Nb (approximately 2.5 at.%); however, Nb was not observed in the Cu phase, leading to observations of asymmetry in forced mixing. The EDS area scan analysis inside the Nb particle results in an average Cu concentration of 2.55 at.% (Fig. 5d$_3$).

Path 2 microstructural characterization

SEM and STEM microstructural analyses of Cu–Nb consolidate processed via path 2 are presented in Fig. 6. A light micrograph of the vertical cross-section of the consolidate processed via path 2 is shown in Fig. 6a, wherein a processing depth of 2.90 mm is observed. The processed region consists of banded microstructural evolution, and representative images are shown in the inset of Fig. 6a and Fig. 6b$_1$. The high-magnification image of the banded region in Fig. 6b$_2$ shows that the Nb particles are not completely resolved due to the resolution limit of the SEM. Furthermore, a qualitative SEM–EDS analysis indicates that the region contained 1–2 at.% of Nb, as shown in Fig. 6d. Microstructural analysis outside the banded region is presented in Fig. 6b$_3$. The following are the key attributes of the Path 2 microstructure: (1) Cu grains (as marked by solid arrows), (2) coarse Nb particles, and (3) deformed Nb particles (marked by dotted arrows in Fig. 6b$_3$). Based on these observations, the banded regions are more heavily deformed compared with the region outside the bands. To further understand the microstructural evolution in the heavily deformed bands, a FIB lift-out was made from the region marked by the solid rectangle in Fig. 6b$_2$. The corresponding STEM analysis is presented in Fig. 6c$_1$–c$_3$. The Cu grains are elongated and extremely strained. Furthermore, the presence of twinning is also noted as marked by solid arrows in Fig. 6c$_1$. In addition to microstructural imaging, STEM-EDS mapping was carried out to understand the distribution of the Nb particles, and the results are presented in Fig. 6c$_2$, c$_3$. In these images, Nb particles are refined and uniformly distributed in the Cu matrix. The analyzed region exhibits a Nb concentration of 0.6 at.% (Fig. 6d).
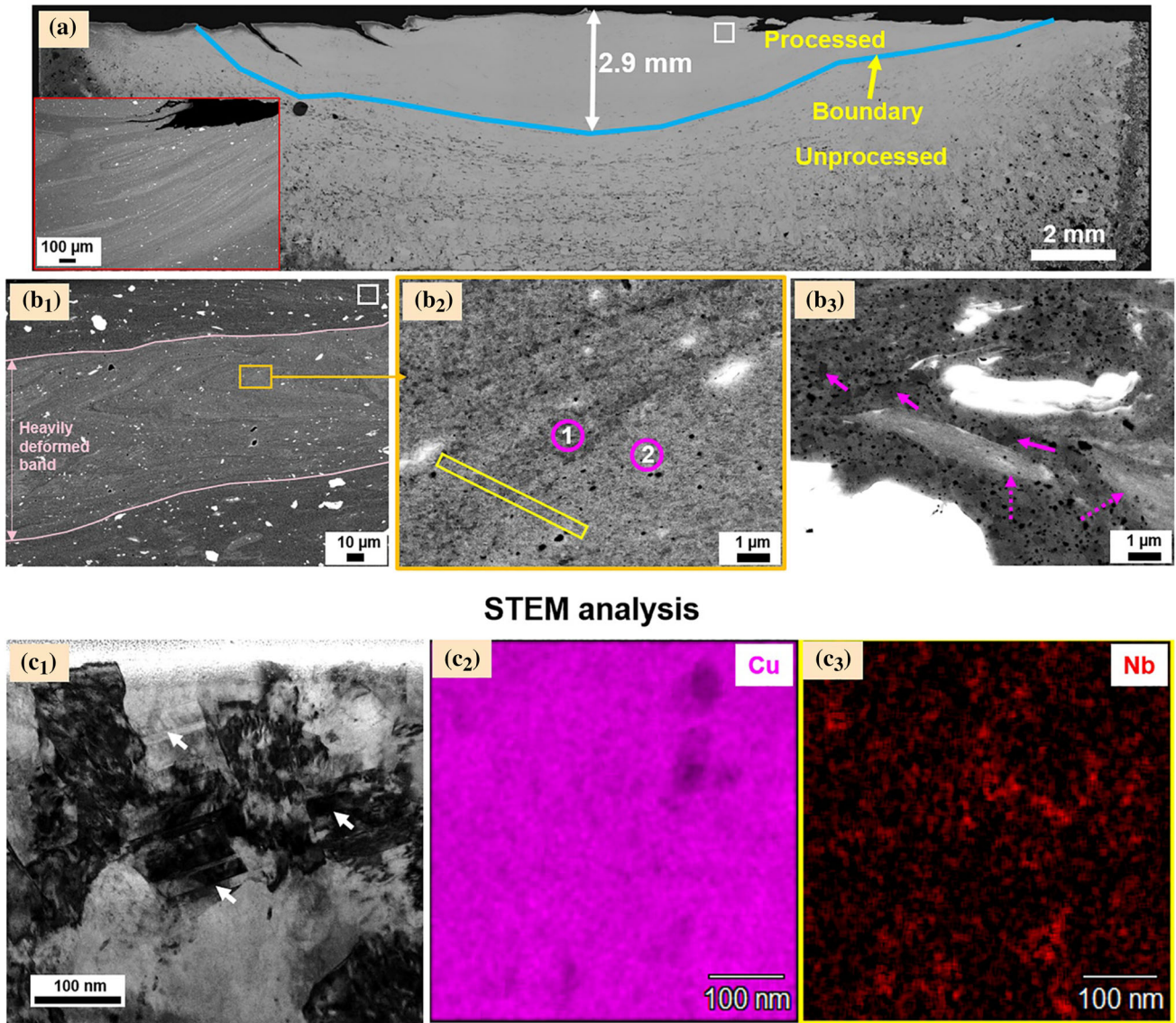
STEM analysis

EDS analysis	SEM		STEM
	1 (b₂)	2 (b₂)	Area (c₂ and c₃)
Cu (at.%)	98.9	97.8	99.40
Nb (at.%)	1.1	2.2	0.60

Figure 6 Microstructural analyses of the friction consolidated sample processed via path 2. **a** Light microscopy image showing the vertical cross-section, BSE-SEM images of the processed region showing **b₁** an overview consisting of banded microstructural evolution, **b₂** high-magnification BSE image of the heavily deformed region, and **b₃** deformed Nb particle outside the banded structure. Solid rectangle in (**b₂**) shows the location of the TEM sample. **c₁** STEM-BF shows the heavily deformed Cu with extensive deformation twins (marked by arrows) and STEM-EDS maps of **c₂** Cu and **c₃** Nb showing the distribution of Nb phase in the Cu matrix. The darker regions in (**c₂**) are of Fe-rich. **d** Summary of SEM–EDS spot analysis of the four locations marked in (**b₂**) and (**b₃**) and quantification of STEM-EDS area analysis of the region presented in (**c₂**) and (**c₃**). (For color coding, please refer to the online version).

XRD analysis of Cu–Nb

The fine Nb banding shown in Fig. 6b$_1$ was of particular interest, and micro-XRD analysis was performed to further investigate the microstructural evolution. The XRD analysis of the Cu–Nb consolidate processed via path 2 in comparison with the unprocessed material is presented in Fig. 7. The observed phases were Cu, Nb, and Cu$_2$O. The main observation is that the Nb peaks shifted towards higher angles, while Cu peak positions remained unchanged in the processed region compared with the unprocessed material. The lattice parameter of Nb before and after processing was 3.3114 and 3.3037 Å, respectively. This agrees with the observed presence of Cu in the Nb lattice. Furthermore, the following equation can be used to obtain the Cu concentration in Nb [11]:

$$C_{Cu}^{Nb} = \frac{(a^3/a_0^3) - 1}{(\Delta V/V)_{Cu}^{Nb}} \tag{1}$$

where C_{Cu}^{Nb} is the concentration of Cu in Nb, a and a_0 are the lattice parameter of Nb alloy and the lattice parameter of Nb before the consolidation process. $(\Delta V/V)_{Cu}^{Nb}$ is the relative volume change resulting from the introduction of one Cu solute atom into the Nb lattice. The volume changes for Cu in Nb and Nb in Cu are −0.25 and 1.1, respectively [16]. The calculation in Eq. (1) yields an average Cu concentration of 2.80 at.% that is in solid solution with Nb. However, even at 1000 K, the maximum equilibrium solubility of Cu in Nb is about 0.15 at.%, denoting the formation of forced supersaturated solubility via friction consolidation under Path 2 conditions.

Discussion

In the following section, the microstructural evolution observed in the two deformation pathways in comparison with other extreme shear deformation techniques will be carried out, followed by an examination of possible mechanisms to explain the observed asymmetric mixing. The primary findings are: (1) significant microstructural refinement is noted for both deformation pathways, (2) significant differences in microstructural evolution exist between the two pathways (Fig. 8), and (3) an asymmetry in forced mixing is noted with Cu in Nb but not vice versa.

Figure 7 XRD analysis of Cu–Nb before and after the friction consolidation process (path 2). Data collected using Cr radiation (λ = 2.2897 Å).
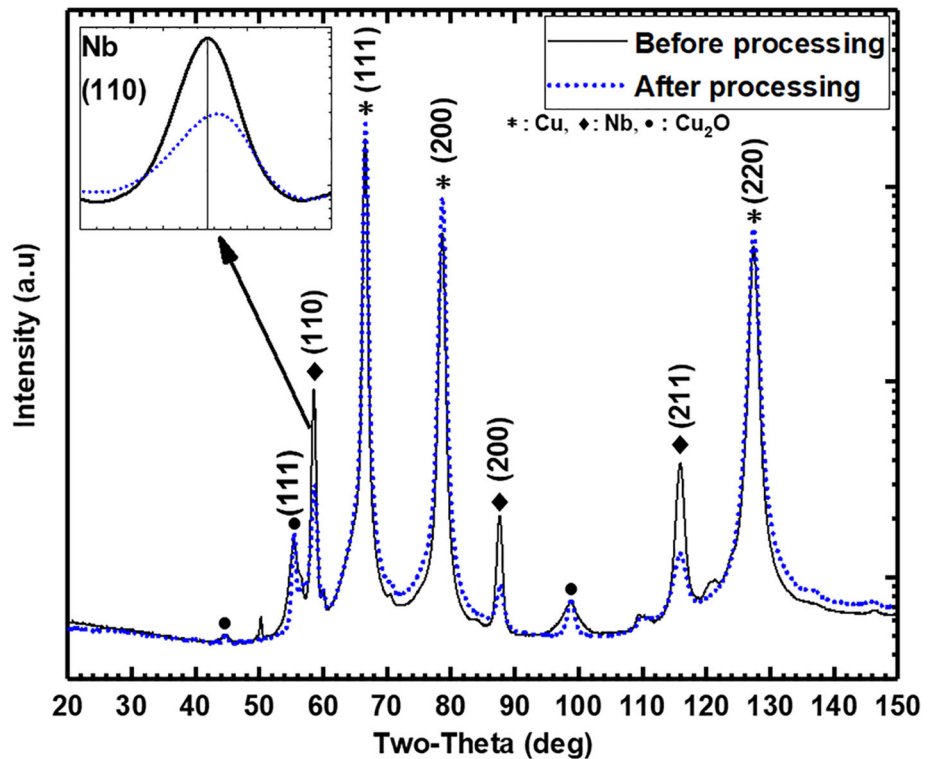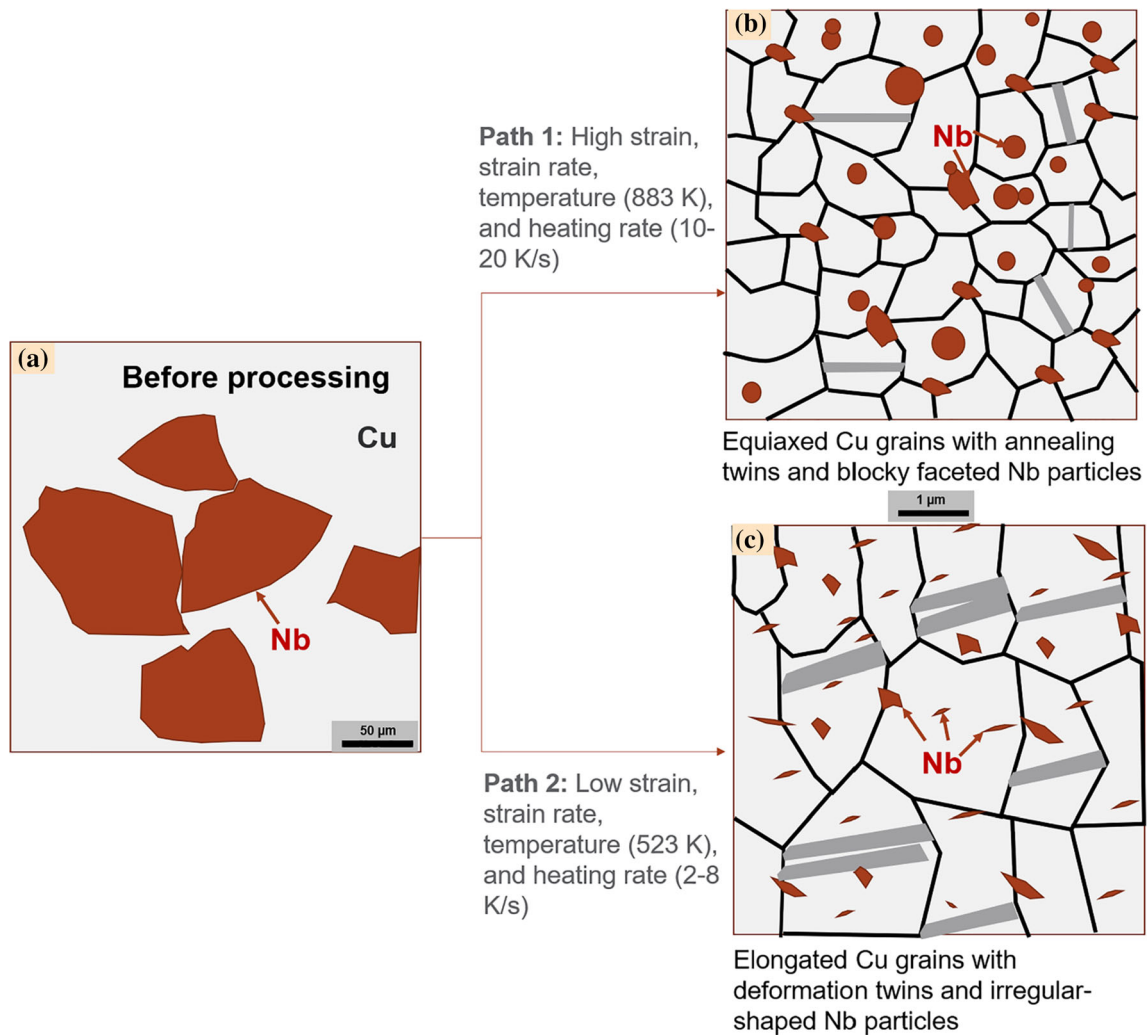
Figure 8 Schematic illustration of microstructural evolution in the high (Path 1) and low (Path 2) strain pathways in the Cu–Nb alloy. (For color coding, please refer to the online version).

Microstructural evolution in friction consolidated samples

In the current investigation, path 1 demonstrates the microstructural evolution for high strain, strain rate, and temperature processing, while path 2 reveals the microstructural evolution at low strain and temperature processing. Please note that the evolved microstructures do not represent the steady-state microstructure due mainly to high temperature and shorter time of the friction consolidation process. Further processing might lead to slightly different microstructures as compared with the current observations and will potentially reach steady state with respect to constant processing temperature and microstructure. The observed microstructures in this investigation represent a point in the temperature–time pathway. This is in contrast with HPT processing where steady-state microstructure is achieved after total shear strain of 3000 (about 100 HPT turns) [48]. Furthermore, both paths 1 and 2 friction consolidation processes were repeated, and SEM analysis concluded similar microstructural evolution making the process reproducible. In path 1, equiaxed ultrafine Cu grains with annealing twins, agglomerated Nb particles located along grain boundaries, and Nb particle sizes generally above 10 nm in the grain interior are observed. The presence of Nb particles along the grain boundary restricts boundary movement due mainly to Zener pinning, while the nanocrystalline Nb particles inside the Cu grain provide effective obstacles to dislocation movement, thereby enhancing strength and thermal stability

[1, 30]. In Path 2, elongated Cu grains with high defect density, deformation twinning, and highly dispersed Nb particles below 10 nm in the heavily deformed banded region are noted. The larger Nb particle size in path 1 compared to path 2 reveals the effect of thermal diffusion on the Nb particle size evolution, even during processing. The non-spherical Nb particles below 50 nm in path 2 imply ongoing deformation and continued microstructural evolution. The schematic in Fig. 8 summarizes the key differences in the microstructural evolution between the high and low strain deformation pathways. Microstructural evolution in the Cu–Nb model system under extreme shear deformation conditions has been investigated via various experimental [8, 9, 11, 14, 31] and simulation [15–19] efforts. For instance, after low and room temperature HPT processing, Nb particles reached a steady-state particles size of ∼ 10 nm and 26–42 nm, respectively, providing some indication of the effect of temperature on the steady-state Nb particle size [9, 31].

Extended solubility of Nb in Cu was noted in previous investigations employing HPT [9, 11, 31] and wire drawing [10, 14] techniques, although to a varying extent. For instance, approximately 1 and 2–3 at.% of Nb in Cu was noted in samples deformed via HPT at room temperature [31] and at 195 K (using dry ice cooling) [9], while significantly higher Nb fractions were observed in a wire drawing [14] experiment. The noted differences could be due to the variations in the imposed deformation conditions and total strain. As noted, temperature had a significant effect on the evolution of the HPT microstructures with lower-temperature deformation pathway leading to relatively higher extended solubility. Further effects of temperature on the microstructural evolution during an SPD process can be clearly seen from MD simulations of an alloy with a positive heat of mixing [17]. Up to 500 K, the microstructure retained the starting random solution with the short-range order parameter (Ω) close to zero, whereas processing at 800 and 1000 K resulted in a Ω value close to −1 signifying the decomposition of the solid solution. It is noted that the experiments that reported extended solubility were conducted at or below room temperature. In the current investigation, path 1 and path 2 microstructures underwent final processing temperatures of ∼ 883 and ∼ 523 K, respectively. Nb enrichment in Cu was not observed in either of these two pathways. An important factor to consider in the case of forced mixing is that temperature will ultimately destabilize the supersaturated solid solution. Therefore, in the case of the friction consolidation process, if there was enhanced forced mixing during the process due to elevated processing temperatures, the Nb or Cu solutes could precipitate out in the respective matrix, albeit at different destabilizing temperature. Therefore, forced mixing during the deformation cannot be ruled out in path 1. Interestingly, the presence of Cu in Nb was noted in both the pathways, leading to asymmetry in forced mixing across the Cu/Nb interface. Similar asymmetry was noted in Cu–Cr [49], Cu–Nb [11, 14] and Cu–Ag–Nb [10]. For example, in HPT processed Cu–Nb alloy, 11 at.% of Cu in Nb and only 0.80 at.% Nb in Cu was observed at a shear strain of 5970 [11]. The observation was rationalized based on the disparities in the heat of mixing. The heat of mixing-based argument is adequate for non-shear-based processing methods, since it does not fully consider the shear deformation-driven mixing. Furthermore, on the contrary to the experimental observations, results from MD simulations of Cu–Nb noted the presence of Nb atoms in the Cu matrix but no Cu atoms in the Nb particles [17]. This was explained based on the extensive dislocation activity in Cu that transported Nb atoms away from the interface, while limited dislocation activity in the Nb particle diminished the movement of Cu atoms in Nb. Some points that can rationalize the predictions of the MD simulation are: (1) the Nb particles were ∼ 5 nm which would reduce the deformation extent compared with the experimental observations, and (2) the presence of amorphous structure around the Nb particles could change the mixing characteristics at the interface. The simulation results can be applied to the deformation of Nb particles in the nanocrystalline size regime, but much of the structural evolution during the two friction consolidation pathways took place at a much larger length scales. Overall, regardless of the disparity between the experimental and simulation observations on the asymmetric forced mixing, the origin of the asymmetry in forced mixing is not fully understood. A discussion will be presented in the following subsection.

Mechanism of deformation

Various mechanisms have been proposed to explain the forced mixing in otherwise immiscible systems,

including defect-assisted diffusion [24–26], ballistic effects causing superdiffusion [28, 29, 50], dislocation shuffling across the interface and shear banding [10], dissolution of $\sim$ 1–5 nm particles due to capillary forces [25], mixing through grain boundary regions in materials with nanocrystalline grain size, and shear removal of atoms from the particles by the matrix dislocations [15–17]. The last three mechanisms are operative only when the grain/particle sizes are of a few nanometers and hence cannot be used to explain the mixing behavior in coarser grains/particles. Defect-assisted diffusion and ballistic mixing partly explain the mixing process but do not account for the differences in deformation extent and the relative mobilities.

Therefore, in the present work, a hypothesis will be proposed based on deformation conditions, and thermodynamic and kinetic factors, to explain the observed asymmetry in mixing. The hypothesis is presented in Fig. 9 and has two criteria. Criteria I is based on the differences in deformation characteristics of Cu and Nb, and Criteria II is based on the differences in diffusion coefficients. The yield strengths of Cu and Nb at room temperature are 50–80 MPa [51] and 300–350 MPa [52], respectively. Therefore, due to the strength disparity between Cu and Nb, the strength of the Cu should increase via work hardening for effective load transfer and subsequent deformation of the Nb. In the case of a AA1050/AlN composites, an increase in the strength of the Al matrix via strain hardening intensified the stress experienced by the AlN ceramic particles indicating the importance of strain hardening on efficient load transfer [53]. Significant work hardening of Cu was noted up to $\sim$ 573 K [51]. Compared with Cu, the Nb exhibits limited work hardening [52]. As noted in Fig. 3, the process temperature generally increases with increasing processing time which dynamically alters the deformation conditions. Therefore, during the initial deformation stage, there should be significant work hardening of Cu. As the Cu deforms (Fig. 9a), dislocations continue to pile-up at the Cu–Nb interface leading to the increased defect-density along the interface. Due to limited plastic deformation of Nb, the accumulated defect density on the Nb side of the interface will be lower compared with the Cu side (Fig. 9b). This non-uniform deformation alone has the potential to lead to uneven material transfer across the interface, with more Cu atoms traversing the interface into Nb

($\Gamma_{forced}^{Cu \rightarrow Nb} \gg \Gamma_{forced}^{Nb \rightarrow Cu}$) (Fig. 9c). As the friction consolidation process proceeds, the deformation and fracture of the Nb particles will increase the strength of the Cu matrix via composite strengthening. At this point, increasing the processing temperature beyond 573 K and losing the inherent work hardening of Cu should not obstruct further deformation of the Nb.

The main hypothesis for Criteria II is based on the self- and interdiffusion coefficient of Cu and Nb and differences in deformation-induced vacancy concentration between the Cu and Nb (Fig. 9d). Though the equilibrium diffusion coefficients are not accurate to be employed in shear-induced mixing, the thermodynamic aspects might offer an indication of the observed microstructural evolution. At 1000 K, the self-diffusion coefficients of Cu and Nb are 7.8593×10^{-12} cm^2/s and 3.2092×10^{-21} cm^2/s [54], respectively, and interdiffusion coefficients for Cu into Nb [55] and Nb into Cu [56] are 4.7604×10^{-17} cm^2/s and 1.5268×10^{-13} cm^2/s, respectively. The vacancy concentration in Cu near melting is nominally 50×10^{-4}, which is close to the Path 2 vacancy concentration calculated based on the equation. Based on the vacancy concentration calculations, the self-diffusion coefficient near the melting point of Cu is 2.7750×10^{-9} cm^2/s. Since similar information was not available for Nb, a comparatively low vacancy concentration and a small self-diffusion coefficient compared with Cu are assumed. Overall, the Cu self-diffusion is much higher than the interdiffusion of Nb into Cu, thus the fraction of Nb diffusing into Cu would be extremely small. Based on the above estimations, the probability of Cu atoms diffusing into Nb would be higher than the reverse case. Furthermore, differences in the heat of mixing (ΔH_m), i.e. ΔH_m for Cu in Nb and Nb in Cu are 46 kJ/mol and 98.7 kJ/mol, respectively, would intensify the asymmetry in material mixing [57].

Overall, the high deformation activity of Cu and subsequent forced mixing, in addition to the large interdiffusion coefficient of Cu in Nb compared with the self-diffusivity of Nb, are expected to result in Cu supersaturation in Nb. Similarly, the low deformation activity of Nb and subsequent reduced forced mixing, in addition to the large self-diffusion coefficient of Cu compared to the interdiffusion coefficient of Nb into Cu, are expected to limit the superdiffusive mixing of Nb into Cu. This hypothesis might also explain the mixing behavior in Cu–Cr and Cu–Fe
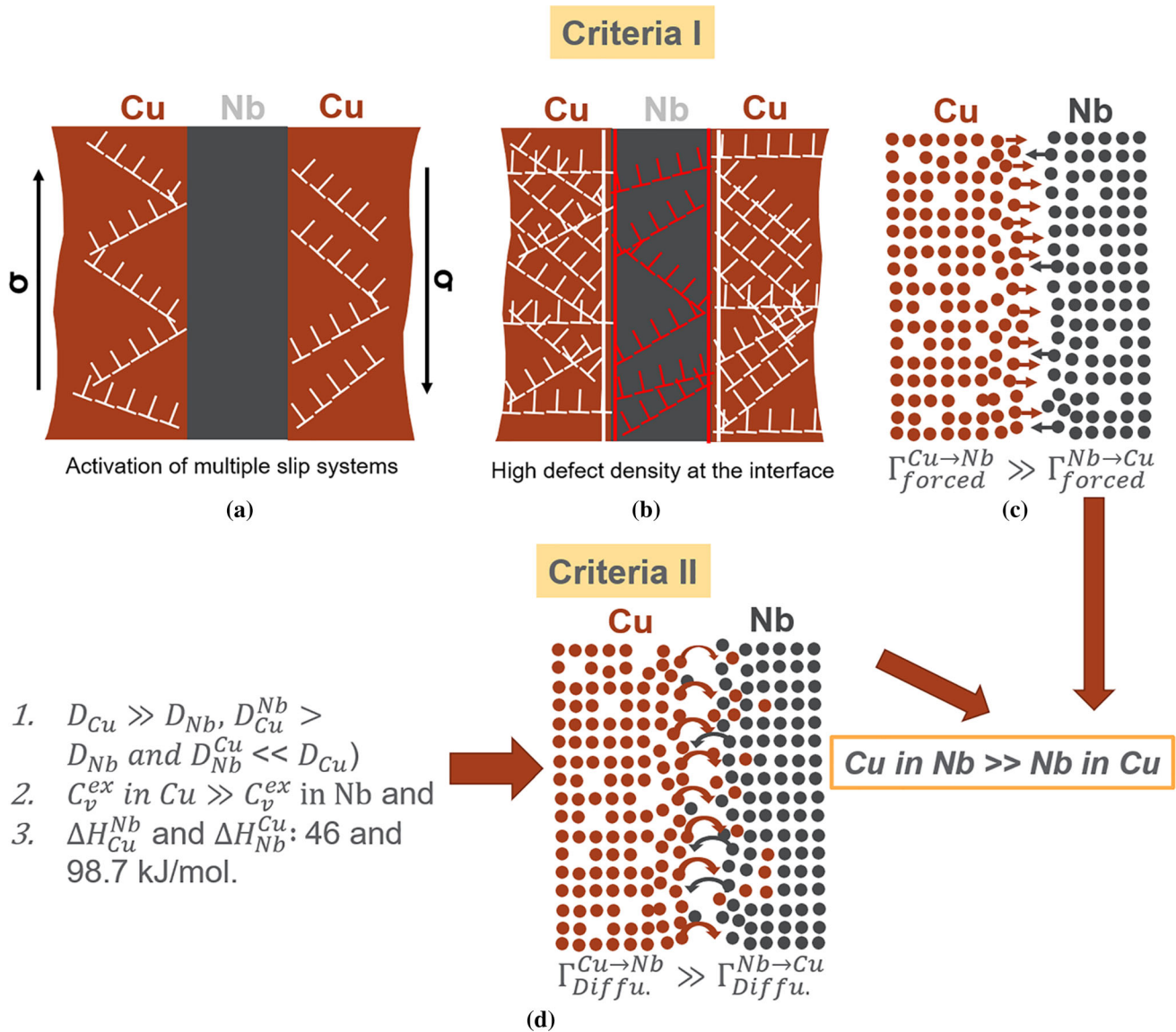
Criteria I

(a) Activation of multiple slip systems

(b) High defect density at the interface

(c) $\Gamma_{forced}^{Cu \to Nb} \gg \Gamma_{forced}^{Nb \to Cu}$

Criteria II

1. $D_{Cu} \gg D_{Nb}, D_{Cu}^{Nb} > D_{Nb}$ and $D_{Nb}^{Cu} \ll D_{Cu})$
2. C_v^{ex} in $Cu \gg C_v^{ex}$ in Nb and
3. ΔH_{Cu}^{Nb} and ΔH_{Nb}^{Cu}: 46 and 98.7 kJ/mol.

(d) $\Gamma_{Diffu.}^{Cu \to Nb} \gg \Gamma_{Diffu.}^{Nb \to Cu}$

Cu in Nb >> Nb in Cu

Figure 9 Schematic explaining the forced superdiffusive mixing leading to asymmetry in composition across the interface. D_{Cu} and D_{Nb}: self-diffusivity of Cu and Nb, respectively, D_{Cu}^{Nb}: interdiffusivity of Cu in Nb, D_{Nb}^{Cu}: interdiffusivity of Nb in Cu, C_v^{ex}: excess vacancy concentration, and ΔH_{Cu}^{Nb} and ΔH_{Nb}^{Cu}: heat of mixing for Cu in Nb and Nb in Cu, respectively. (For color coding please refer to the online version).

immiscible systems. In Cu–Cr, asymmetry in mixing was noted, while Cu–Fe with constituents of similar strength did not have asymmetry after HPT [58].

Summary and concluding thoughts

Elemental Cu and Nb powder blends were subjected to friction consolidation at relatively high (path 1) and low (path 2) plastic strain conditions. Extensive deformation of Nb particles is noted in both

deformation pathways. In path 1, agglomerated Nb particles in the ultrafine-grained Cu matrix are observed, while in path 2 highly dispersed Nb is noted in a heavily deformed Cu matrix. Furthermore, the presence of Cu in Nb particles is noted; however, supersaturation of Nb in Cu is not observed. The occurrence of mixing asymmetry is explained based on differences in the deformation extent of Cu and Nb, the corresponding vacancy concentration and forced mixing disparities. Furthermore, the differences in self- and interdiffusion coefficients for Cu

and Nb may also intensify the variation in extent of mixing across the interface favoring Cu in Nb over Nb in Cu.

The current findings provide a pathway to understand the effect of shear deformation conditions on microstructural evolution in various Cu–X immiscible systems such as Cu–Cr, Cu–Ta, and Cu–Fe. Furthermore, the current observations can broadly be used to interpret the plastic deformation and microstructural evolution of soft matrix and hard second phases under various solid phase processing techniques such as friction extrusion, friction consolidation, and shear assisted processing and extrusion.

Data availability statement

The raw/processed data required to reproduce these findings can be obtained upon a direct request to the corresponding author.

Declaration

References

[1] Tschopp MA, Murdoch HA, Kecskes LJ, Darling KA (2014) Bulk nanocrystalline metals: review of the current state of the art and future opportunities for copper and copper alloys. Jom 66(6):1000–1019

[2] Darling KA, Rajagopalan M, Komarasamy M, Bhatia MA, Hornbuckle BC, Mishra RS, Solanki KN (2016) Extreme creep resistance in a microstructurally stable nanocrystalline alloy. Nature 537(7620):378–381

[3] Vo NQ, Schäfer J, Averback RS, Albe K, Ashkenazy Y, Bellon P (2011) Reaching theoretical strengths in nanocrystalline Cu by grain boundary doping. Scripta Mater 65(8):660–663

[4] Vo NQ, Chee SW, Schwen D, Zhang X, Bellon P, Averback RS (2010) Microstructural stability of nanostructured Cu alloys during high-temperature irradiation. Scripta Mater 63(9):929–932

[5] Komarasamy M, Tharp R, Sinha S, Thapliyal S, Mishra R (2019) Achieving forced mixing in Cu-based immiscible alloys via friction stir processing, friction stir welding and processing X. Springer, Cham, pp 199–208

[6] Sun YF, Fujii H, Nakamura T, Tsuji N, Todaka D, Umemoto M (2011) Critical strain for mechanical alloying of Cu–Ag, Cu–Ni and Cu–Zr by high-pressure torsion. Scripta Mater 65(6):489–492

[7] Kormout KS, Pippan R, Bachmaier A (2017) Deformation-induced supersaturation in immiscible material systems during high-pressure torsion . Adv Eng Mater 19(4)

[8] Botcharova E, Freudenberger J, Schultz L (2004) Mechanical alloying of copper with niobium and molybdenum. J Mater Sci 39(16–17):5287–5290. https://doi.org/10.1023/B:JMSC.0000039230.73188.5d

[9] Beach JA, Wang M, Bellon P, Dillon S, Ivanisenko Y, Boll T, Averback RS (2017) Self-organized, size-selection of precipitates during severe plastic deformation of dilute Cu–Nb alloys at low temperatures. Acta Mater 140:217–223

[10] Raabe D, Ohsaki S, Hono K (2009) Mechanical alloying and amorphization in Cu–Nb–Ag in situ composite wires studied by transmission electron microscopy and atom probe tomography. Acta Mater 57(17):5254–5263

[11] Ekiz EH, Lach TG, Averback RS, Mara NA, Beyerlein IJ, Pouryazdan M, Hahn H, Bellon P (2014) Microstructural evolution of nanolayered Cu–Nb composites subjected to high-pressure torsion. Acta Mater 72:178–191

[12] Mula S, Bahmanpour H, Mal S, Kang PC, Atwater M, Jian W, Scattergood RO, Koch CC (2012) Thermodynamic feasibility of solid solubility extension of Nb in Cu and their thermal stability. Mater Sci Eng A 539:330–336

[13] Komarasamy M, Mishra RS, Mukherjee S, Young ML (2015) Friction stir-processed thermally stable immiscible nanostructured alloys. Jom 67(12):2820–2827

[14] Sauvage X, Renaud L, Deconihout B, Blavette D, Ping D, Hono K (2001) Solid state amorphization in cold drawn Cu/Nb wires. Acta Mater 49(3):389–394

[15] Ashkenazy Y, Pant N, Zhou J, Bellon P, Averback RS (2017) Phase evolution of highly immiscible alloys under shear deformation: kinetic pathways, steady states, and the lever-rule. Acta Mater 139:205–214

[16] Ashkenazy Y, Vo NQ, Schwen D, Averback RS, Bellon P (2012) Shear induced chemical mixing in heterogeneous systems. Acta Mater 60(3):984–993

[17] Vo NQ, Odunuga S, Bellon P, Averback RS (2009) Forced chemical mixing in immiscible alloys during severe plastic deformation at elevated temperatures. Acta Mater 57(10):3012–3019

[18] Vo NQ, Averback RS, Ashkenazy Y, Bellon P, Wang J (2012) Forced chemical mixing at Cu–Nb interfaces under severe plastic deformation. J Mater Res 27(12):1621–1630

[19] Odunuga S, Li Y, Krasnochtchekov P, Bellon P, Averback RS (2005) Forced chemical mixing in alloys driven by plastic deformation. Phys Rev Lett 95(4):045901

[20] Vo NQ, Zhou J, Ashkenazy Y, Schwen D, Averback RS, Bellon P (2013) Atomic mixing in metals under shear deformation. Jom 65(3):382–389

[21] Schwen D, Wang M, Averback RS, Bellon P (2013) Compositional patterning in immiscible alloys subjected to severe plastic deformation. J Mater Res 28(19):2687–2693

[22] Wang J, Misra A (2011) An overview of interface-dominated deformation mechanisms in metallic multilayers. Curr Opin Solid State Mater Sci 15(1):20–28

[23] Bellon P, Averback RS (1995) Nonequilibrium roughening of interfaces in crystals under shear: application to ball milling. Phys Rev Lett 74(10):1819–1822

[24] Gente C, Oehring M, Bormann R (1993) Formation of thermodynamically unstable solid solutions in the Cu–Co system by mechanical alloying. Phys Rev B Condens Matter 48(18):13244–13252

[25] Quelennec X, Menand A, Le Breton JM, Pippan R, Sauvage X (2010) Homogeneous Cu–Fe supersaturated solid solutions prepared by severe plastic deformation. Phil Mag 90(9):1179–1195

[26] Khina BB, Formanek B (2006) Mathematical modeling of solid-state diffusion during mechanical alloying. Defect Diffusion Forum 249:105–110

[27] Xu J, He J, Ma E (1997) Effect of milling temperature on mechanical alloying in the immiscible Cu–Ta system. Metall Mater Trans A 28(7):1569–1580

[28] Martin G (1984) Phase stability under irradiation: ballistic effects. Phys Rev B 30(3):1424–1436

[29] Lund AC, Schuh CA (2003) Driven alloys in the athermal limit. Phys Rev Lett 91(23):235505

[30] Sinha S, Komarasamy M, Thapliyal S, Gwalani B, Shukla S, Darling KA, Mishra RS (2019) Immiscible nanostructured copper-aluminum-niobium alloy with excellent precipitation strengthening upon friction stir processing and aging. Scripta Mater 164:42–47

[31] Wang M, Averback RS, Bellon P, Dillon S (2014) Chemical mixing and self-organization of Nb precipitates in Cu during severe plastic deformation. Acta Mater 62:276–285

[32] Carpenter J, Vogel S, LeDonne J, Hammon D, Beyerlein I, Mara NA (2012) Bulk texture evolution of Cu–Nb nanolamellar composites during accumulative roll bonding. Acta Mater 60(4):1576–1586

[33] Ma E (2005) Alloys created between immiscible elements. Prog Mater Sci 50(4):413–509

[34] Suryanarayana C (2001) Mechanical alloying and milling. Prog Mater Sci 46(1–2):1–184

[35] Li X, Tang W, Reynolds AP, Tayon WA, Brice CA (2016) Strain and texture in friction extrusion of aluminum wire. J Mater Process Technol 229:191–198

[36] Fihey J, Nguyen-Duy P, Roberge R (1976) On the solidification microstructure of copper-rich niobium alloys. J Mater Sci 11(12):2307–2311. https://doi.org/10.1007/BF00752095

[37] Lavender CA, Joshi VV, Grant GJ, Jana S, Whalen SA, Darsell JT, Overman NR (2019) System and process for formation of extrusion products. US Patent No. 10,189,063, 29 Jan 2019

[38] Overman NR, Whalen SA, Bowden ME, Olszta MJ, Kruska K, Clark T, Stevens EL, Darsell JT, Joshi VV, Jiang X, Mattlin KF, Mathaudhu SN (2017) Homogenization and texture development in rapidly solidified AZ91E consolidated by shear assisted processing and extrusion (ShAPE). Mater Sci Eng A 701:56–68

[39] Whalen S, Joshi V, Overman N, Caldwell D, Lavender C, Skszek T (2017) Scaled-up fabrication of thin-walled ZK60 tubing using shear assisted processing and extrusion (ShAPE). In: Magnesium technology, vol 2017, pp 315–321

[40] Whalen S, Overman N, Joshi V, Varga T, Graff D, Lavender C (2019) Magnesium alloy ZK60 tubing made by shear

assisted processing and extrusion (ShAPE). Mater Sci Eng A 755:278–288

[41] Joshi VV, Jana S, Li D, Garmestani H, Nyberg E, Lavender C (2014) High shear deformation to produce high strength and energy absorption in Mg alloys. In: Magnesium technology, vol 2014, pp 83–88

[42] Jiang X, Whalen SA, Darsell JT, Mathaudhu S, Overman NR (2017) Friction consolidation of gas-atomized FeSi powders for soft magnetic applications. Mater Charact 123:166–172

[43] Catalini D, Kaoumi D, Reynolds AP, Grant GJ (2013) Friction Consolidation of MA956 powder. J Nucl Mater 442(1–3):S112–S118

[44] Overman N, Li X, Olszta M, Nickerson E, Overman C, Mathaudhu S, Grant G, Whalen S (2020) Microstructural progression of shear-induced mixing in a CuNi alloy. Mater Charact 110759.

[45] Li X, Overman N, Roosendaal T, Olszta M, Zhou C, Wang H, Perry T, Schroth J, Grant G (2019) Microstructure and mechanical properties of pure copper wire produced by shear assisted processing and extrusion. Jom 71(12):4799–4805

[46] Tang W, Reynolds AP (2010) Production of wire via friction extrusion of aluminum alloy machining chips. J Mater Process Technol 210(15):2231–2237

[47] Mishra RS, De PS, Kumar N (2014) Friction stir processing, friction stir welding and processing. Springer, Cham, pp 259–296

[48] Stückler M, Krenn H, Kürnsteiner P, Gault B, De Geuser F, Weissitsch L, Wurster S, Pippan R, Bachmaier A (2020) Intermixing of Fe and Cu on the atomic scale by high-pressure torsion as revealed by DC- and AC-SQUID susceptometry and atom probe tomography. Acta Mater 196:210–219

[49] Bachmaier A, Aboulfadl H, Pfaff M, Mucklich F, Motz C (2015) Structural evolution and strain induced mixing in Cu–

Co composites studied by transmission electron microscopy and atom probe tomography. Mater Charact 100:178–191

[50] Ma E, Sheng H, He J, Schilling P (2000) Solid-state alloying in nanostructured binary systems with positive heat of mixing. Mater Sci Eng, A 286(1):48–57

[51] Abed FH, Voyiadjis GZ (2007) Thermodynamic consistent formulations of viscoplastic deformations in FCC metals. J Eng Mech 133(1):76–86

[52] Nemat-Nasser S, Guo W (2000) Flow stress of commercially pure niobium over a broad range of temperatures and strain rates. Mater Sci Eng A 284(1–2):202–210

[53] Reddy AC (2015) Necessity of strain hardening to augment load bearing capacity of AA1050/AlN nanocomposites. Int J Adv Res 3(6):1211–1219

[54] Kraftmakher Y (1998) Equilibrium vacancies and thermophysical properties of metals. Phys Rep 299(2–3):79–188

[55] Ablitzee D (1977) Diffusion of niobium, iron, cobalt, nickel and copper in niobium. Philos Mag J Theor Exp Appl Phys 35(5):1239–1256

[56] Butrymowicz DB, Manning JR, Read ME (1974) Diffusion in copper and copper alloys, part II. Copper-silver and copper-gold systems. J Phys Chem Ref Data 3(2):527–602

[57] Chakrabarti D (1979) The Cu–Nb (Copper–Niobium) system. Phys Rev B 29:133787

[58] Bachmaier A, Kerber M, Setman D, Pippan R (2012) The formation of supersaturated solid solutions in Fe–Cu alloys deformed by high-pressure torsion. Acta Mater 60(3):860–871